and three in the vertical direction. Conservation of angular momentum dictates that the tangential velocity of the orbiting molecules is modulated at the radial betatron oscillation frequency as well. The experimental data in the upper trace of Fig. 4 demonstrates that a bunch of ammonia molecules with a velocity of 89 m s^{-1} can still be identified after it has made six round trips in the storage ring. The observed gradual broadening and decrease in peak intensity after each additional round trip is largely explained by the above-mentioned spreading out of the package along the ring, as substantiated by the results from Monte Carlo simulations, shown in the lower trace of Fig. 4. Loss of molecules from the storage ring by collisions with background gas can explain the observed faster decay of signal at early times after the gas pulse, when the background pressure is still rather high. Unwanted transitions to states that are degenerate in zero field—another possible loss channel for the ring—are avoided in the chosen electric-field geometry.

The storage ring experimentally demonstrated here can generally be used to confine dipolar molecules. The advantage of a storage ring over a trap is that bunches of cold molecules in a ring can be made to interact repeatedly, at well defined times and at distinct locations, with electromagnetic fields and/or other particles. A sectional version of the storage ring allows implementation of field-free interaction regions and various out-coupling regions. This yields unique opportunities for high-resolution molecular spectroscopy as well as for a large variety of collision studies. By incorporating a re-bunching element in the ring, the gradual spreading out of the package that is observed now can be avoided and the stored molecules can be confined to the same region in phase-space for a time-period only limited by collisions with background gas. Different molecules can be stored simultaneously; slowly overtaking or counter-propagating bunches can be stored and used for collision studies. The excellent optical access to the storage ring makes it feasible to use laser detection schemes to accurately determine where the molecules are in the ring at each given moment in time. If this is done in a non-intrusive manner, for instance via two-level laser-induced fluorescence or by detecting the change in refractive index when they pass through an optical cavity, this information can be used to actively correct the trajectories of individual molecules towards the ideal, circular orbit, thus increasing the phase-space density of the stored molecules (stochastic cooling[8]). It is important to note that in the ring, molecules in high-field-seeking states can also be stored[15]; motional stabilization as demonstrated here can also be used to stabilize orbits of particles that, according to the Earnshaw theorem, cannot be trapped in a static geometry. Whenever any cooling scheme on the stored molecules is proved to work (stochastic cooling, evaporative cooling, laser cooling on ro-vibrational transitions, cavity-mediated cooling[16]), reloading of the ring will be possible. Such reloading might be a viable way of achieving phase-space densities of stored molecules that are sufficiently high to permit experimental study of molecular quantum-collective effects. ☐

Received 15 January; accepted 23 March 2001.

1. Kügler, K.-J., Paul, W. & Trinks, U. A magnetic storage ring for neutrons. *Phys. Lett. B* **72,** 422–424 (1978).
2. Niel, L. & Rauch, H. Acceleration, deceleration and monochromatization of neutrons in time dependent magnetic fields. *Z. Phys. B* **74,** 133–139 (1989).
3. Huffman, P. R. *et al.* Magnetic trapping of neutrons. *Nature* **403,** 62–64 (2000).
4. Weinstein, J. D., deCarvalho, R., Guillet, T., Friedrich, B. & Doyle, J. M. Magnetic trapping of calcium monohydride molecules at millikelvin temperatures. *Nature* **395,** 148–150 (1998).
5. Bethlem, H. L., Berden, G. & Meijer, G. Decelerating neutral dipolar molecules. *Phys. Rev. Lett.* **83,** 1558–1561 (1999).
6. Bethlem, H. L., Berden, G., van Roij, A. J. A., Crompvoets, F. M. H. & Meijer, G. Trapping neutral molecules in traveling potential well. *Phys. Rev. Lett.* **84,** 5744–5747 (2000).
7. Bethlem, H. L. *et al.* Electrostatic trapping of ammonia molecules. *Nature* **406,** 491–494 (2000).
8. van der Meer, S. Stochastic damping of betatron oscillations in the ISR. CERN internal report CERN/ISR-PO/72-31 (CERN, Geneva, 1972).
9. Katz, D. P. A storage ring for polar molecules. *J. Chem. Phys.* **107,** 8491–8501 (1997).
10. Weiner, J., Bagnato V. S., Zilio, S. & Julienne, P. S. Experiments and theory in cold and ultracold collisions. *Rev. Mod. Phys.* **71,** 1–85 (1999).
11. Gupta, M. & Herschbach, D. A mechanical means to produce intense beams of slow molecules. *J. Phys. Chem. A* **103,** 10670–10673 (1999).
12. Gandhi, S. R. & Bernstein, R. B. Focusing and state selection of NH_3 and OCS by the electrostatic hexapole via first- and second-order Stark effects. *J. Chem. Phys.* **87,** 6457–6467 (1987).
13. Lee, S. Y. Accelerator physics. (World Scientific, Singapore, 1999).
14. Ashfold, M. N. R., Dixon, R. N., Little, N., Stickland, R. J. & Western, C. M. The $\tilde{B}'E''$ state of ammonia: sub-Doppler spectroscopy at vacuum ultraviolet energies. *J. Chem. Phys.* **89,** 1754–1761 (1988).
15. Loesch, H. J. & Scheel, B. Molecules on Kepler orbits: an experimental study. *Phys. Rev. Lett.* **85,** 2709–2712 (2000).
16. Vuletić, V. & Chu, S. Laser cooling of atoms, ions, or molecules by coherent scattering. *Phys. Rev. Lett.* **84,** 3787–3790 (2000).

Acknowledgements

This work is part of the research programme of the Stichting voor Fundamenteel Onderzoek der Materie (FOM), which is financially supported by the Nederlandse Organisatie voor Wetenschappelijk Onderzoek (NWO). The research of R.T.J. has been made possible by a fellowship of the Royal Netherlands Academy of Arts and Sciences. We acknowledge the expert technical assistance of A.J.A. van Roij, and the help of G. Berden and J. Ye in the experiments. G. M. dedicates this work to P. Andresen.

Correspondence and requests for information should be addressed to G.M.
(e-mail: gerardm@rijnh.nl).

Evidence against dust-mediated control of glacial–interglacial changes in atmospheric CO_2

B. A. Maher*† **& P. F. Dennis***

* *Centre for Environmental Magnetism and Palaeomagnetism (CEMP) and Stable Isotope Laboratory, School of Environmental Sciences, University of East Anglia, Norwich NR4 7TJ, UK*

The low concentration of atmospheric CO_2 inferred to have been present during glacial periods is thought to have been partly caused by an increased supply of iron-bearing dust to the ocean surface[1]. This is supported by a recent model[2] that attributes half of the CO_2 reduction during past glacial stages to iron-stimulated uptake of CO_2 by phytoplankton in the Southern Ocean. But atmospheric dust fluxes to the Southern Ocean, even in glacial periods, are thought to be relatively low and therefore it has been proposed that Southern Ocean productivity might be influenced by iron deposited elsewhere—for example, in the Northern Hemisphere[3,4]—which is then transported south via ocean circulation (similar to the distal supply of iron to the equatorial Pacific Ocean[5–7]). Here we examine the timing of dust fluxes to the North Atlantic Ocean, in relation to climate records from the Vostok ice core in Antarctica around the time of the penultimate deglaciation (about 130 kyr ago). Two main dust peaks occurred 155 kyr and 130 kyr ago, but neither was associated with the CO_2 rise recorded in the Vostok ice core. This mismatch, together with the low dust flux supplied to the Southern Ocean, suggests that dust-mediated iron fertilization of the Southern Ocean did not significantly influence atmospheric CO_2 at the termination of the penultimate glaciation.

The Southern Ocean is a 'high nutrient, low chlorophyll' (HNLC) region; phosphate and nitrate concentrations are high at the ocean surface yet its productivity is low. Recent experiments show that artificial additions of iron to ocean patches significantly enhance primary productivity[8], with consequent drawdown of surface water

---

† Present address: CEMP, Lancaster Environment Centre, Department of Geography, University of Lancaster, LA1 4YP, UK.

f_{CO_2}: the water becomes a sink for atmospheric CO_2. Hence, the strength of the 'biological pump' may influence atmospheric CO_2 concentrations. The Vostok (Antarctic) ice-core record shows that towards the end of past glacial stages, the Southern Ocean region warmed and atmospheric CO_2 levels rose several thousand years before the Northern Hemisphere ice sheets melted. Thus, this region may greatly influence and/or amplify climate change. A major control on iron supply to HNLC regions is thought to be the flux of terrestrial dust[1,2]. A model[2] of the ocean–atmosphere carbon cycle, which predicts up to 40 p.p.m. CO_2 drawdown in response to increased Southern Ocean dust flux during glacial stages, used a modelled[9] estimate of modern dust flux of 14 mg cm^{-2} kyr^{-1} (a value considered over-estimated[9]) and a Last Glacial Maximum (LGM) value of 345 mg cm^{-2} kyr^{-1}. Data on the present-day dust flux to the Southern Ocean, although sparse, are mutually consistent[10–12] and indicate much lower fluxes of 0.1–1 mg cm^{-2} kyr^{-1}. At glacial times, increased aridity and/or wind strength could have contributed to higher Southern Ocean dust fluxes and thus to lower atmospheric CO_2 concentrations. The Vostok record indeed shows peak dust flux during glaciations, when atmospheric CO_2 was depressed by about 80 p.p.m. (ref. 13). However, geological data indicate that these increased glacial dust fluxes were small, and negligible compared with detrital (non-aeolian) sediment accumulation rates in the Southern Ocean. The Southern Ocean exhibits sedimentation rates far greater than the atmospheric flux, owing to bottom-water transport of detritus. For Scotia Sea sediments, for example, the aeolian contribution from the South American loess regions (identified isotopically as the principal source of Vostok's dust[14]) is below the level of detection, even during glacial periods[15]. Similarly, in cores from the southeast Indian Ocean to the Antarctic continental slope, aeolian particles account for less than 10% of the clay minerals present[16]. An aeolian flux 600 times greater than that actually recorded in the Vostok ice core ($\sim$2 mg cm^{-2} kyr^{-1}) would be required to explain the lithogenic flux at these sites during glacial times[16]. Thus, the interpretation of lithogenic accumulation rates as a proxy for Southern Ocean dust flux[17] seems to be invalid. Similarly, dust concentration changes in the Vostok ice core cannot be used to constrain model simulations of past dust fluxes[2] because snow accumulation rates were lower during glacial stages; hence dust flux changes were much smaller than concentration changes[9].

Given the low dust fluxes to this region, iron supply from upwelling water seems to be a more significant source, by at least an order of magnitude[3,4]. Similar upwelled iron supply has been identified for the HNLC region of the equatorial Pacific[5–7]. Thus, for the Southern Ocean, upwelled iron and resultant productivity may

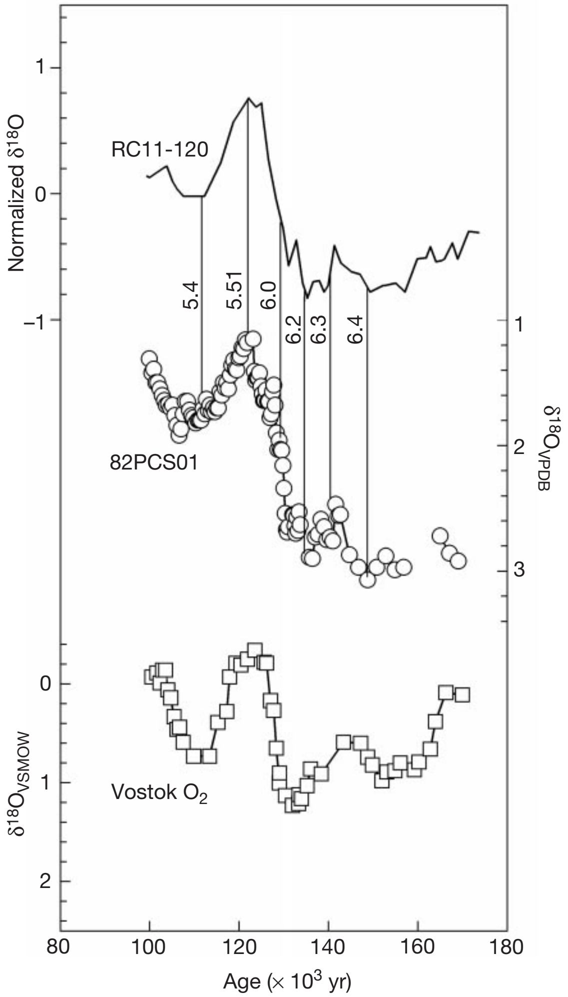

Figure 1 The high-resolution foraminiferal (*Globorotalia bulloides*) oxygen isotope record for piston core 82PCS01 (42° 05′ N 23° 31′ W, water depth 3,540 m). The chronology is based on the indicated tie points between the measured data and the orbitally tuned deep sea record of core RC11-120 (ref. 21). The oxygen isotope substages are marked on the tie lines. The Vostok δ^{18}O (in air)[13], measured with respect to Vienna Standard Mean Ocean Water (VSMOW), is plotted using the GT4 timescale. For the 100–170 kyr period represented by these records, the chronology is in excellent agreement with an independent age model based on orbital tuning of both the marine and Vostok records to tilt and precession cycles[22].

reflect distal (that is, Northern Hemisphere), rather than Southern Hemisphere, dust inputs. It has been suggested that iron from the peri-Saharan region (the largest dust source in the world) may be transported in southward flow of the North Atlantic intermediate/deep water to the circumpolar region, on a timescale of approximately 100 yr (refs 3, 4). This hypothesis suggests that the pattern of Northern, rather than Southern, Hemisphere dust flux may match more closely the pattern and timing of CO_2 variations recorded by the Vostok ice core.

Here we test this hypothesis by high-resolution oxygen isotope, magnetic and elemental analysis of a deep-sea sediment record, core 82PCS01, from the abyssal plain northeast of the Azores. Sedimentation at this site has been continuous and undisturbed from oxygen isotope stage (OIS) 8 to the present day[18]. The core site lies above the lysocline, precluding carbonate dissolution, and underlies the present northern margin of the Bermuda–Azores high-pressure system, around which African dust can be transported northwards in the summer[19]. Upon sinking, possible complexation or dissolution[20], iron may become entrained within southward-flowing Atlantic intermediate/deep water. We obtained an age model for the core via oxygen isotope analysis of the planktonic foraminifer, *Globorotalia bulloides*, correlating the data with the chronostratigraphy of ref. 21. We measured the magnetic remanence acquired at high applied magnetic fields (the HIRM) of the sediments, as a proxy for iron. Additional analyses on subsets of samples included carbonate content, elemental iron and dry bulk density. From these data, we calculated sedimentation rates and fluxes of iron and dust.

Figure 1 shows the oxygen isotope data for core 82PCS01, with the chronology based on tie points to the high-resolution chronostratigraphy[21]. Also shown in Fig. 1 is the Vostok $\delta^{18}O$ (in air) record[13]. Both these chronologies agree strongly (to within 1 kyr) with the one newly derived by tuning the benthic marine $\delta^{18}O$ record (and the Vostok air $\delta^{18}O$ record) to tilt and precession cycles[22]. Figure 2 shows the $\delta^{18}O$ and HIRM data for core 82PCS01, for the time interval 100–170 kyr ago. For comparison, terrigenous percentage data are also shown for another, more southerly core in the eastern Atlantic. core 82PCS01 appears to record a representative (but much higher resolution) signal of dust input over at least a regional scale. For glacial stage 6, core 82PCS01 displays two peaks in HIRM, at approximately 130 kyr and ~155 kyr ago. For the succeeding interglacial stage, from about 125 kyr to 100 kyr ago, HIRM values are low and less variable. These high-resolution data amplify those reported[23] for gravity cores in this area. Goethite, a significant component of soils within the semi-arid zone, has been identified as the major contributor to the HIRM of these sediments[23]. Given the saturation remanence of goethite[24] ($\sim 0.05\,\mathrm{A\,m^2\,kg^{-1}}$), our carbonate-free HIRM values ($7\text{–}44 \times 10^{-4}\,\mathrm{A\,m^2\,kg^{-1}}$) indicate goethite concentrations in the dust component of the sediment of 1.4–8.8%. HIRM values (for every sample) and independently determined iron (in wt%, determined for a subset of samples) are directly and strongly correlated ($R^2 = 0.83$). Thus, rapid, non-destructive HIRM measurements appear to be a robust proxy for aeolian, elemental iron concentrations in these North Atlantic sediments. It should be noted that our North Atlantic record shows particulate iron deposition through time, rather than dissolved iron. The relationship between iron-bearing dust flux and dissolved iron concentrations in deep water is unknown, but dust-sourced increases in deep-water iron would imply increased concentrations of organic ligands capable of complexing the iron to maintain solubility[20].

Figure 3a shows the calculated dust fluxes for core 82PCS01, for the period spanning glacial stage 6, Termination II and interglacial stage 5. Dust flux was 3–5 times higher during two intervals: about 155 kyr ago ($\sim 5\,\mathrm{g\,cm^{-2}\,kyr^{-1}}$) and about 130 kyr ago ($\sim 3\,\mathrm{g\,cm^{-2}\,kyr^{-1}}$). During interglacial stage 5 (from ~130 kyr ago on), dust fluxes decreased rapidly before steadying at about $1\,\mathrm{g\,cm^{-2}\,kyr^{-1}}$. For comparison, estimates of modern fluxes[9] for the northeast equatorial Atlantic mostly range from $0.2\text{–}3\,\mathrm{g\,cm^{-2}\,kyr^{-1}}$, with (depending on latitude) a one- to four-fold increase in dust flux at the Last Glacial Maximum.

The oxygen isotope records from 82PCS01 and Vostok are in excellent agreement (Fig. 1 and Fig. 3d and e). At Termination II, the rise in $\delta^{18}O$ (in air) at Vostok lags the North Atlantic rise by about 2 kyr; this delay is attributable to the Dole effect[22]. The major, five-fold increase in our North Atlantic dust flux is thus virtually synchronous with peak A in the Vostok dust concentration record (Fig. 3c). However, at its peak, the Vostok dust flux is about 2,500 times smaller than our North Atlantic flux ($\sim 2\,\mathrm{mg\,cm^{-2}\,kyr^{-1}}$ compared with $5\,\mathrm{g\,cm^{-2}\,kyr^{-1}}$). In global climate terms, this large rise and fall in North Atlantic dust (and iron) flux occurred entirely within OIS 6, with little apparent variation in either atmospheric CO_2 or oxygen isotope values (Fig. 3d–g). North Atlantic dust flux then declined, substantially earlier (by ~7,000 yr) than the onset of the CO_2 rise at Vostok. The second dust flux event in core 82PCS01, centred on about 130 kyr ago, may have provided a significant, later supply of iron to drive Southern Ocean productivity, when Southern Hemisphere dust flux had diminished to near-zero. However, as shown in Fig. 3, this subsidiary peak in dust flux significantly post-dates (by ~7,000 years) the onset of the CO_2 rise. Rather than being associated with draw-down of CO_2 and maintenance of glacial conditions, the peak of this later event coincides with a marked, 1‰ shift in deep-sea oxygen isotope values (Fig. 3d), indicating either

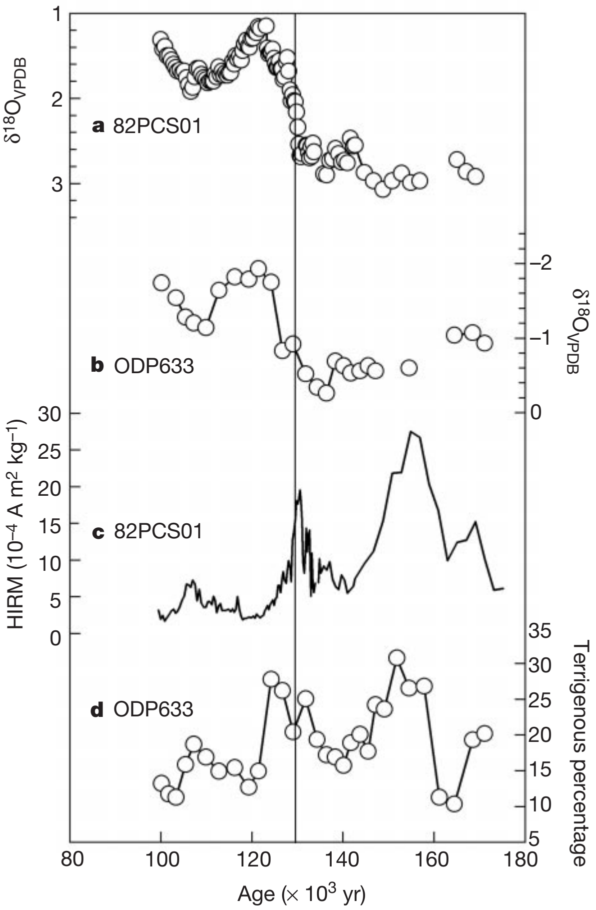

Figure 2 Oxygen isotope and dust (HIRM and terrigenous percentage) records from the eastern North Atlantic. **a**, Oxygen isotope data for piston core 82PCS01, 8.8 m of carbonate ooze interbedded with marly ooze; **b**, oxygen isotope data for Ocean Drilling Program hole 633 (ref. 27), from the eastern tropical Atlantic (1.2° N 11.9° W); **c**, HIRM data for core 82PCS01; **d**, published terrigenous percentage values for ODP hole 663 (ref. 27). The vertical line represents Termination II at about 130 kyr ago[21].

warming North Atlantic sea surface temperatures[25] and/or melting of the Northern Hemisphere ice sheets.

Thus, although fluxes of Northern Hemisphere dust may constitute an alternative, higher-magnitude supply of iron to the Southern Ocean, they seem to bear no causal relationship with either changes in Southern Ocean temperature or atmospheric CO_2, as recorded at Vostok around Termination II. These data—the evidence of very low dust fluxes to the Southern Ocean, and the mismatch of timing between the Northern Hemisphere flux peaks and Southern Ocean climate change—thus do not appear to support the suggested role of dust-mediated iron fertilization in the Southern Ocean at and around the Termination II boundary. ☐

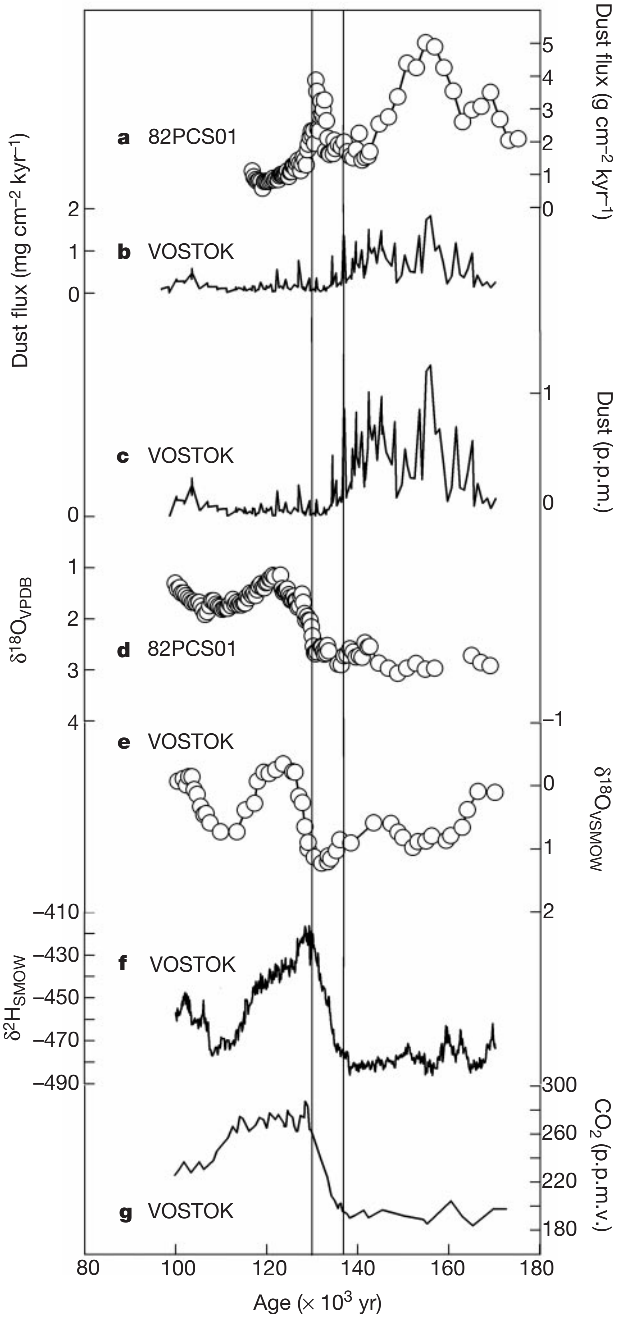

Figure 3 Dust, isotopic and CO_2 records from the North Atlantic and the Vostok ice core. **a**, Dust flux values for core 82PCS01; **b**, dust flux values for the Vostok ice core (ref. 13; J. R. Petit, personal communication); **c**, dust concentration in the Vostok ice core[13]; **d**, oxygen isotope data for piston core 82PCS01; **e**, oxygen isotope data (in air) in the Vostok ice core[13]; **f**, deuterium data for the Vostok ice core[13]; **g**, CO_2 data for the Vostok ice core[13]. The vertical lines at 137 kyr and 130 kyr mark the onset of the CO_2 rise recorded at Vostok (137 yr) and the Termination II boundary (130 kyr).

Methods

From each 1-cm sample (sieved at 63 μm), 10–20 adult specimens (0.2–0.5 mg) of the planktonic foraminifer, *Globorotalia bulloides*, were picked for oxygen isotope analysis. These were reacted off-line with 102% orthophosphoric acid at 25 °C for 12 h; the evolved CO_2 was dried by passing through a cold trap at −90 °C and cryodistilled into gas sample tubes. Isotopic analyses were performed on a VG SIRA series II dual-inlet isotope ratio mass spectrometer. Oxygen isotopic compositions, with respect to the Vienna Pee-Dee Belemnite (VPDB) standard, are accurate and precise to better than 0.1‰. Analysis of 0.2-mg aliquots of the internal laboratory standard run at random with the foraminiferal samples, at an average frequency of 1 in 4 samples, have a precision ($1\sigma_{n-1}$) of ±0.06‰ ($n = 30$). For magnetic analysis, the fraction of each sample less than 63 μm was dried and packed into 10-cm^3 plastic cylinders. Magnetic fields were generated using a pulse magnetizer (up to 100 mT) and electromagnet (up to 1 T); magnetic remanences were measured using a fluxgate magnetometer (sensitivity ≈ 10^{-7} A m^2). Carbonate content was obtained by gasometry, and elemental iron content by X-ray fluorescence of sample beads, fused with sodium lithoborate.

To calculate the iron flux F_{Fe}, the following equation was used: $F_{Fe} = r_s \rho_{db} p$, where flux is in units of g cm^{-2} kyr^{-1} and r_s = sedimentation rate (cm kyr^{-1}), ρ_{db} = dry bulk density (g cm^{-3}) and p is the weight fraction of iron.

From the age model, a sedimentation rate was calculated for each sediment depth. Heavy sampling meant it was not possible to obtain a ρ_{db} value for every sample depth. Density was estimated[26] from the relationship between $CaCO_3$ content and the measured ρ_{db} of a subset of samples (14) spanning the $CaCO_3$ range. For values of p, the weight fraction of iron was estimated for every sample from the HIRM/elemental iron correlation. Dust flux was calculated from the p value, assuming an average iron abundance in mineral aerosols of 3.5% (ref. 10).

Received 23 August 2000; accepted 5 March 2001.

1. Martin, J. H. Glacial-interglacial CO_2 change; the iron hypothesis. *Paleoceanography* **5,** 1–13 (1990).
2. Watson, A. J., Bakker, D. C. E., Ridgwell, A. J., Boyd, P. W. & Law, C. S. Effect of iron supply on Southern Ocean CO_2 uptake and implications for glacial atmospheric CO_2. *Nature* **407,** 730–733 (2000).
3. Watson, A. J. & Lefevre, N. The sensitivity of atmospheric CO_2 concentrations to input of iron to the oceans. *Tellus B* **51,** 453–460 (1999).
4. Lefevre, N. & Watson, A. J. Modelling the geochemical cycle of iron in the oceans and its impact on atmospheric carbon dioxide concentrations. *Glob. Biogeochem. Cycles* **13,** 727–736 (1999).
5. Loubere, P. Marine control of biological production in the eastern equatorial Pacific Ocean. *Nature* **406,** 497–500 (2000).
6. Coale, K. H., Fitzwater, S. E., Gordon, R. M., Johnson, K. S. & Barber, R. T. Control of community growth and export production by upwelled iron in the equatorial Pacific Ocean. *Nature* **379,** 621–624 (1996).
7. Wells, M. L., Vallis, G. K. & Silver, E. A. Tectonic processes in Papua New Guinea and past productivity in the eastern equatorial Atlantic. *Nature* **398,** 601–604 (1999).
8. Boyd, P. W. *et al.* A mesoscale phytoplankton bloom in the polar Southern Ocean stimulated by iron fertilization. *Nature* **407,** 695–702 (2000).
9. Mahowald, N. *et al.* Dust sources and deposition during the last glacial maximum and current climate: A comparison of model results with paleodata from ice cores and marine sediments. *J. Geophys. Res.* **104,** 15895–15916 (1999).
10. Duce, R. & Tindale, N. W. Atmospheric transport of iron and its deposition in the ocean. *Limnol. Oceanogr.* **42,** 405–418 (1991).
11. Husar, R. B., Prospero, J. M. & Stowe, L. L. Characterization of tropospheric aerosols over the oceans with the advanced very high resolution radiometer optical thickness operation product, NOAA. *J. Geophys. Res.* **102,** 16889–16901 (1997).
12. Measures, C. I. & Vink, S. On the use of dissolved aluminium in surface waters to estimate dust deposition to the ocean. *Glob. Biogeochem. Cycles* **14,** 317–327 (2000).
13. Petit, J. R. *et al.* Climate and atmospheric history of the past 420 000 years fro the Vostok ice core, Antarctica. *Nature* **399,** 429–436 (1999).
14. Basile, I. *et al.* Patagonian origin of glacial dust deposited in East Antarctica (Vostok and Dome C) during glacial stages 2, 4 and 6. *Earth Planet. Sci. Lett.* **146,** 573–589 (1997).
15. Diekmann, B. *et al.* Terrigenous sediment supply in the Scotia Sea (Southern Ocean): response to late Quaternary ice dynamics in Patagonia and on the Antarctic Peninsula. *Palaeogeogr. Palaeoclimatol. Palaeoecol.* **162,** 357–388 (2000).
16. Bareille, G., Grousset, F. E. & Labracherie, M. Origin of detrital fluxes in the southeast Indian Ocean during the last climatic cycles. *Paleoceanography* **9,** 799–819 (1994).
17. Kumar, N. *et al.* Increased biological productivity and export production in the glacial Southern Ocean. *Nature* **378,** 675–680 (1995).
18. Kidd, R. B. *et al.* King's Trough Flank: geological and geophysical investigations of its suitability for high-level radioactive waste disposal. *Inst. Oceanogr. Sci. Rep.* **166,** 1–98 (1983).
19. Reiff, J., Forbes, G., Spieksma, F. & Reynders, J. African dust reaching northwestern Europe: A case study to verify trajectory calculations. *J. Clim. Appl. Meteorol.* **25,** 1543–1567 (1986).
20. Jickells, T. D. & Spokes, L. J. in *The Biogeochemistry of Iron in Seawater* (eds Turner, G. & Hunter, K. A.) (Wiley, New York, in the press).
21. Martinson, D. G. *et al.* Age dating the orbital theory of the Ice Ages: Development of a high-resolution 0 to 300,000 years chronostratigraphy. *Quat. Res.* **27,** 1–29 (1987).
22. Shackleton, N. J. The 100,000 year ice-age cycle identified and found to lag temperature, carbon dioxide and orbital eccentricity. *Science* **289,** 1897–1902 (2000).
23. Robinson, S. G. The late Pleistocene palaeoclimatic record of North Atlantic deep-sea sediments revealed by mineral magnetic measurements. *Phys. Earth Planet. Inter.* **42,** 22–47 (1986).

24. Maher, B. A. & Thompson, R. in *Quaternary Climates, Environments and Magnetism* (eds Maher, B. A. & Thompson, R.) 1–48 (Cambridge Univ. Press, Cambridge, UK, 1999).
25. Chapman, M. R. & Shackleton, N. J. Millennial-scale fluctuations in North Atlantic heat flux during the last 150,000 years. *Earth Planet. Sci. Lett.* **159,** 57–70 (1998).
26. Hovan, S. A., Rea, D. K. & Pisias, N. G. Late Pleistocene continental climate and oceanic variability recorded in Northwest Pacific sediments. *Paleoceanography* **6,** 349–370 (1991).
27. DeMenocal, P. B., Ruddiman, W. F. & Pokras, E. M. Influences of high-latitude and low-latitude processes on African terrestrial climate—Pleistocene eolian records from Equatorial Atlantic-Ocean drilling Program Site-663. *Paleoceanography* **8,** 209–242 (1993).

Acknowledgements

We are grateful to Southampton Oceanography Centre for allowing sampling of Core 82PCS01. We also thank K. Miller for picking the foraminifera, and S. Dennis and G. McIntosh for performing oxygen isotope and magnetic analyses, respectively.

Correspondence and requests for materials should be addressed to B.M.
(e-mail: b.maher@lancaster.ac.uk).

Delayed triggering of the 1999 Hector Mine earthquake by viscoelastic stress transfer

Andrew M. Freed* & Jian Lin†

* *Department of Terrestrial Magnetism, Carnegie Institution of Washington, Washington DC 20015, USA*
† *Department of Geology and Geophysics, Woods Hole Oceanographic Institution, Woods Hole, Massachusetts 02543 USA*

Stress changes in the crust due to an earthquake can hasten the failure of neighbouring faults and induce earthquake sequences in some cases[1–5]. The 1999 Hector Mine earthquake in southern California (magnitude 7.1) occurred only 20 km from, and 7 years after, the 1992 Landers earthquake (magnitude 7.3). This suggests that the Hector Mine earthquake was triggered in some fashion by the earlier event. But uncertainties in the slip distribution and rock friction properties associated with the Landers earthquake have led to widely varying estimates of both the magnitude and sign of the resulting stress change that would be induced at the location of the Hector Mine hypocentre—with estimates varying from −1.4 bar (ref. 6) to +0.5 bar (ref. 7). More importantly, coseismic stress changes alone cannot satisfactorily explain the delay of 7 years between the two events. Here we present the results of a three-dimensional viscoelastic model that simulates stress transfer from the ductile lower crust and upper mantle to the brittle upper crust in the 7 years following the Landers earthquake. Using viscoelastic parameters that can reproduce the observed horizontal surface deformation following the Landers earthquake, our calculations suggest that lower-crustal or upper-mantle flow can lead to postseismic stress increases of up to 1–2 bar at the location of the Hector Mine hypocentre during this time period, contributing to the eventual occurrence of the 1999 Hector Mine earthquake. These results attest to the importance of considering viscoelastic processes in the assessment of seismic hazard[8–11].

Earthquake triggering relationships have typically been quantified by changes in Coulomb stress occurring coseismically, $\Delta\sigma_f = \Delta\tau + \mu'\Delta\sigma_n$, where $\Delta\tau$ is the change in shear stress in the slip direction of the receiver fault, $\Delta\sigma_n$ is the change in normal stress (tension positive), and μ' is the apparent coefficient of friction incorporating the influence of pore pressure. Numerous studies have shown good correlations between calculated positive coseismic stress changes and the locations of aftershocks[1,2,12–15] as well as triggering of moderate to large earthquakes[2–5,16,17]. For example, the 1933 Long Beach and 1952 Kern County earthquakes were calculated to have increased coseismic stress in the region of the 1971 San Fernando earthquake, which in turn may have increased coseismic stress at the sites of the 1987 Whittier Narrows and 1994 Northridge events[16].

A limitation of the coseismic stress models is that they only consider elastic responses to fault slip, and thus cannot account for delay times in the triggering process. One possible source for postseismic stress changes is viscous relaxation. Previous analyses have shown that viscous flow in the lower crust or upper mantle after a moderate or major earthquake can lead to significant increases in stress and strain in the seismogenic upper crust, causing it eventually to become the main layer storing strains associated with the original rupture[8–11]. Geodetic studies have revealed rapid regional-scale changes in surface deformation following the Landers earthquake[18–22]. Though a host of processes—including fault-zone collapse[19], afterslip[18,20] and poroelastic rebound[23]—may influence postseismic surface deformation, viscous flow in either the lower crust[24,25] or (predominantly) the upper mantle[26] appears to best explain the observed horizontal surface deformation following the Landers earthquake. Although the viscous-upper-mantle model does a better job of explaining the observed vertical surface deformation[26], the viscous-lower-crust model is more consistent with petrological arguments that a felsic lower crust should be closer to its melting point and therefore weaker than a mafic upper mantle[27]. We therefore consider both rheologies in our calculations of postseismic stress changes.

The June 1992 Landers earthquake, moment magnitude M_w = 7.3, was part of an earthquake sequence that began with the April 1992 M_w = 6.1 Joshua Tree preshock and continued with the M_w = 6.2 Big Bear aftershock only a few hours after the Landers rupture[28] (Fig. 1). To investigate the influence of viscous dissipation following the Landers sequence, we developed a three-dimensional, viscoelastic, finite-element model of a portion of the southern California lithosphere (Fig. 2). Our model considers fault slip associated with the Landers sequence in accordance with slip distributions inferred by the combined inversion of strong motion, teleseismic motion and geodetic data[29]. Previous coseismic analyses of the Landers earthquake approximated the complex rupture surface by mapping slip distributions to three or four linear fault segments[1,2,6,7]. Changes in Coulomb stress are, however, sensitive to kinks and jumps in the slip distribution. This is especially true for the Hector Mine hypocentre that is located only 20 km from the region of maximum slip (5–6 m) during the Landers earthquake, where rupture jumped from the Emerson to the Homestead Valley segments[28] (Fig. 1b). To achieve the best possible accuracy of the calculated coseismic stress changes, we therefore mapped the inferred Landers slip distribution onto fault geometry dictated by observed surface breaks[28] (Fig. 2c).

The reasonableness of our Landers slip model is demonstrated by the good correspondence between the calculated coseismic Coulomb stress increases and the observed aftershocks (Fig. 1). Specifically, the model predicts the location of aftershock clusters, which are especially diagnostic of Landers stress changes as opposed to more randomly distributed normal background seismicity. Of particular interest in Fig. 1b is the region of calculated positive coseismic stress change that extends to the northeast of Landers, encompassing a cluster of aftershocks that occurred near the subsequent Hector Mine epicentre. The occurrence of this aftershock cluster implies crustal weakness near the subsequent Hector Mine rupture site, suggesting that even though coseismic stress changes were not sufficient to trigger the Hector Mine earthquake, the triggering threshold was probably close. Reasonable agreement between our Coulomb stress results and aftershock locations is achieved by assuming an apparent friction coefficient in the range $0.2 < \mu' < 0.6$, with $\mu' = 0.4$ for the example shown in Fig. 1. Our